Global and Planetary Change 223 (2023) 104088

Contents lists available at ScienceDirect

Global and Planetary Change

journal homepage: www.elsevier.com/locate/gloplacha

Hydroclimate dynamics during the Plio-Pleistocene transition in the northwest Pacific realm

Romain Vaucher [a,b,c,*,1], Christian Zeeden [d,1], Amy I. Hsieh [b,e], Stefanie Kaboth-Bahr [f], Andrew T. Lin [g], Chorng-Shern Horng [h], Shahin E. Dashtgard [b]

[a] Institute of Earth Sciences (ISTE), University of Lausanne, Geopolis, CH-1015 Lausanne, Switzerland
[b] Paleoclimate Records in Shallow Marine Strata (PRISMS), Department of Earth Sciences, Simon Fraser University, Burnaby, Canada
[c] Department of Earth Sciences, University of Geneva, Rue des Maraîchers 13, 1205 Geneva, Switzerland
[d] Leibniz Institute for Applied Geophysics (LIAG), Geozentrum Hannover, Hannover, Germany
[e] Department of Geosciences, National Taiwan University, Taipei, Taiwan
[f] Institute of Geosciences, University of Potsdam, Potsdam-Golm, Germany
[g] Department of Earth Sciences, National Central University, Taoyuan, Taiwan
[h] Institute of Earth Sciences, Academia Sinica, Taipei, Taiwan

ARTICLE INFO

Editor: Dr. Alan Haywood

Keywords:
Sea level
Monsoon
Tropical cyclone
Cyclostratigraphy
Sediment flux
Taiwan

ABSTRACT

The appraisal of sedimentary archives is key for predicting sea level changes and extreme weather event behavior under varying greenhouse gas levels. Here, we assess the hydroclimate variability of the northwest Pacific realm during the Pliocene-Pleistocene transition by using a continuous record of gamma-ray log data from two boreholes comprising shallow-marine strata in the Western Foreland Basin, Taiwan. The gamma-ray records provide a high temporally resolved stratigraphic record spanning from ~3.15 to ~1.95 million years ago. The comparison of the astronomically tuned gamma-ray logs to global sea-level and regional sea-surface temperature reconstructions highlights the impact of high- and low-latitude climate drivers on depositional cycles during the Plio-Pleistocene transition. During the late Pliocene, the interplay between the orbitally paced East Asian Summer Monsoon and tropical cyclones dominates the fluctuation in sediment supplied from Taiwan to our study sites. With the intensification of Northern Hemisphere glaciation from the late Pliocene through the early Pleistocene, sea-level changes were ruled by increasingly pronounced glacial-interglacial cycles, and the sedimentary record during this time interval is paced initially by obliquity and later by precession. This study reveals that shallow marine strata can record a more complex history of past hydroclimatie dynamics in the northwest Pacific than recorded in deep sea climate archives.

1. Introduction

During the late Pliocene mean annual surface temperatures were ~3–4 °C warmer than preindustrial values and atmospheric carbon dioxide concentrations ranged between 365 and 415 ppm (Pagani et al., 2009; Haywood et al., 2013; Burke et al., 2018). Sea-level reconstruction from the late Pliocene suggests a maximum of +6 to +14 m during interglacial periods and a minimum of −12 to −26 m during glacial intervals compared to present-day global mean sea level (Berends et al., 2021). At that time, it is suggested that El Niño-like conditions prevailed in the western Pacific due to a weaker Walker Circulation (Kaboth-Bahr and Mudelsee, 2022), and sea surface temperatures in the Western Pacific averaged 28.5 °C (Li et al., 2011). The most favorable conditions for tropical cyclone (TC) genesis across the Cenozoic occurred during the late Pliocene in the northwestern Pacific (Yan et al., 2019). For all these features, the Pliocene climate is considered as a possible analog for near-future Earth's climate in the global warming context (Burke et al., 2018). While Northern Hemisphere ice sheets started expanding in the middle Miocene, the long-term trend of Cenozoic cooling led to an intensification of ice-sheet development during the early Pleistocene (Shackleton et al., 1990; Clark et al., 1999; Zachos et al., 2001). This intensification occurred at ~2.58 Ma with more prominent glacial-interglacial climate variability (Lisiecki and Raymo, 2007). During the early Pleistocene, the global mean annual temperature decreased due to the intensification of

* Corresponding author at: Institute of Earth Sciences (ISTE), University of Lausanne, Geopolis, CH-1015 Lausanne, Switzerland.
E-mail address: romain.vaucher88@gmail.com (R. Vaucher).
[1] The authors equally contributed to this work.

https://doi.org/10.1016/j.gloplacha.2023.104088
Received 27 September 2022; Received in revised form 21 February 2023; Accepted 3 March 2023
Available online 7 March 2023

glacial cycles, and this was manifested in sea-level variations of 25–50 m (Berends et al., 2021). Also, during the early Pleistocene La Niña-like conditions seemed to dominate in the western Pacific (Kaboth-Bahr and Mudelsee, 2022).

Here, we analyze gamma ray (GR) records of Pliocene–Pleistocene shallow-marine strata from two boreholes drilled in the Western Foreland Basin (WFB), Taiwan (Fig. 1). These GR records are used to derive hydroclimate variability (i.e., glacial-interglacial cycles, monsoon activity) between ~3.15 and ~1.95 Ma in the northwest Pacific realm. For this purpose, we: i) built an age-model by combining magneto-biostratigraphic information and astronomical tuning of the GR data to the deep-sea stable oxygen isotope ($\delta^{18}O$) record with an established time scale (Wilkens et al., 2017); and, ii) compared our tuned datasets to state-of-the-art global sea-level reconstructions (i.e., high-latitude climate forcing) (Berends et al., 2021) and to regional sea-surface temperature estimates from the northwest Pacific (i.e., low-latitude climate forcing) (Li et al., 2011). The latter is done to derive hydroclimate trends during the Plio-Pleistocene transition and to assess how they are expressed stratigraphically.

Paleoclimate reconstructions from the sedimentary record provide fundamental data to constrain forecast modeling for Earth's future climate system. Since elevated and rapidly increasing greenhouse gas emissions cause warming of Earth (Zeebe et al., 2016), it is urgent to understand how Earth's surface processes respond to climate changes, especially under warmer than present conditions (Pancost, 2017; Burke et al., 2018). The vast majority of climate narratives from Earth's history (e.g., sea-surface temperature, sea-level reconstruction) are derived from deep-sea archives (e.g., Zachos et al., 2001; Lisiecki and Raymo, 2005; Raymo et al., 2006; Grant et al., 2014; Rohling et al., 2014; Berends et al., 2019; Miller et al., 2020; Westerhold et al., 2020; Berends et al., 2021; Drury et al., 2021). The high temporal completeness of deep-sea records (i.e., quasi-continuous sedimentation, limited erosion and sediment bypass) makes them highly accurate geoarchives. Indeed, deep-sea sediment archives have yielded a wealth of robust data on paleoclimate variability over the last millions of years (e.g., Zeeden et al., 2013; Wilkens et al., 2017; Kaboth-Bahr et al., 2021; van der Lubbe et al., 2021; Beaufort et al., 2022). However, most paleoclimate information is derived from proxy data such as foraminiferal $\delta^{18}O$ or Mg/Ca-ratios that may fail to capture past hydroclimate variabilities at the continent-ocean interface (e.g., Vaucher et al., 2021).

Sea-level rise and an increase in extreme weather events, such as TCs, are two major predicted consequences of global warning (Knutson et al., 2010; Coumou and Rahmstorf, 2012; Peduzzi et al., 2012; Zhang et al., 2020; IPCC, 2021). Even though sea-level fluctuations and extreme weather events leave direct sedimentologic and stratigraphic expressions (Catuneanu et al., 2009; MacEachern et al., 2012; Dashtgard et al., 2020; Vaucher et al., 2021; Green et al., 2022), the stratigraphic records of shallow-marine environments are not commonly regarded as

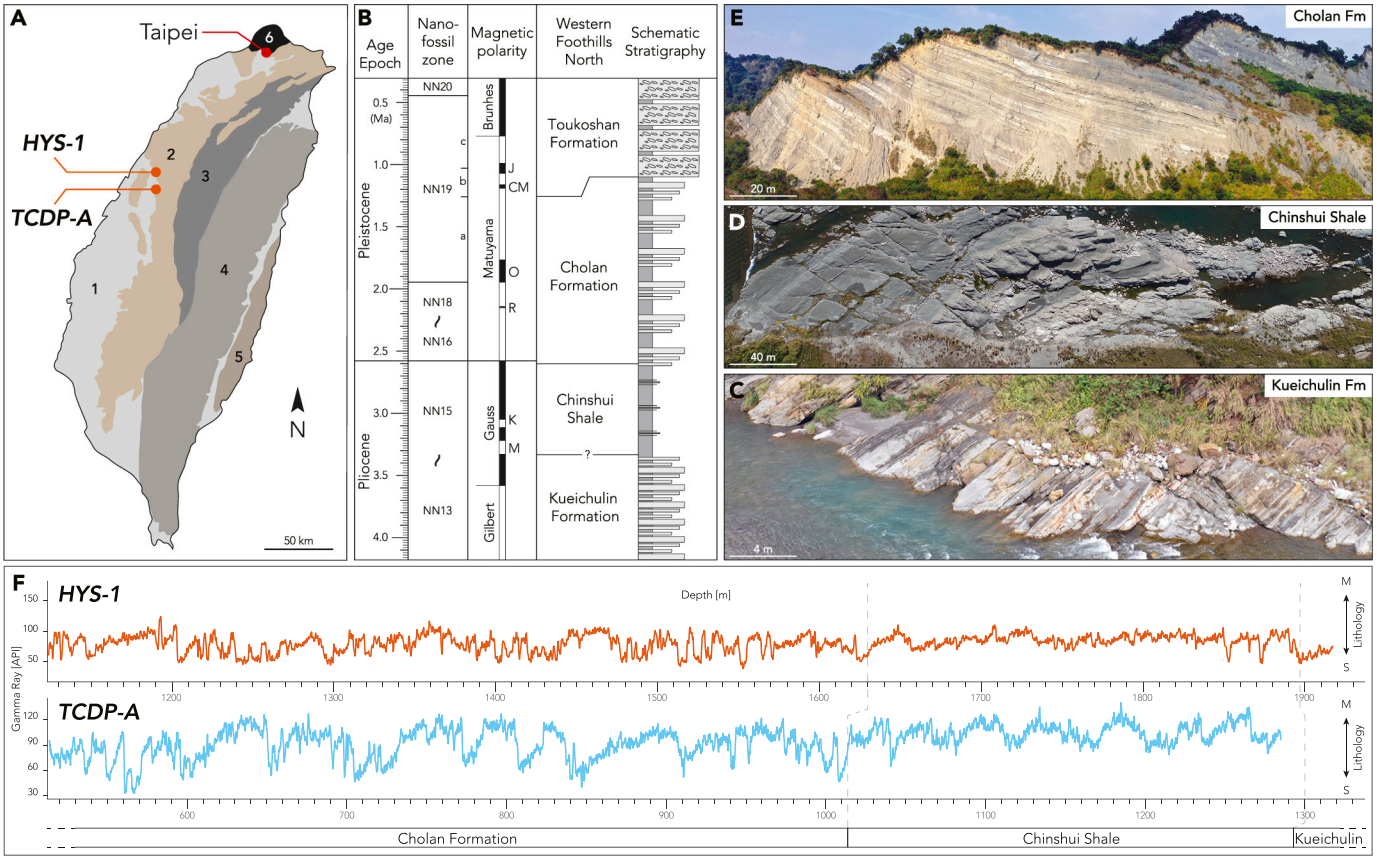

Fig. 1. Geographic and stratigraphic framework. (A) Geological map of Taiwan and the main geological units. 1: Coastal Plain; 2: Western Foothills; 3: Hsuehshan Range; 4: Central Range; 5: Coastal Range; 6: Tatun volcano group (Lin and Chen, 2016). Borehole locations: TCDP-A: 120.73916°E, 24.20083°N, and HYS-1: 120.702024°E, 24.399908°N. (B) The chronostratigraphic chart of the northern part of the Western Foothills and the schematic stratigraphy for the main units. Nanofossils zones and magnetic polarity reversals are shown (Horng and Shea, 2007; Pan et al., 2015; Cohen and Gibbard, 2019; Vaucher et al., 2021). Magnetic polarity abbreviations: J: Jaramillo; CM: Cobb Mountain; O: Olduvai; R: Réunion; K: Kaena; M: Mammoth. The stratigraphic log is not scaled. Dark gray: mudstone-dominated; light gray: sandstone-dominated; light gray with circle: conglomerate-dominated. (C) The sandstone-dominated Kueichulin Formation seen along the Da'an River, Taiwan. (D) The mudstone-dominated Chinshui Shale cropping out along the Ta'Chia River, Taiwan. (E) The heterolithic Cholan Formation marked by a cyclical pattern of deposition exposed along the Wu River, Taiwan. (F) Gamma ray (GR) records acquired from HYS-1 (in orange) and TCDP-A (in light blue) boreholes and their inferred formational limits (modified from Lin et al., 2007). Lithology abbreviation: M: Muddier; S: Sandier. (For interpretation of the references to colour in this figure legend, the reader is referred to the web version of this article.)

excellent climate archives because of their presumed temporal incompleteness (e.g., Barrell, 1917; Sadler, 1981; Jerolmack and Sadler, 2007; Paola et al., 2018). In a recent study, Vaucher et al. (2021) showcase that lower Pleistocene strata in the WFB of Taiwan preserve high-resolution records of past climate oscillations within shallow-marine strata. Deriving such narratives was made possible because of both high accommodation and sedimentation rates in the basin, which enhanced the completeness of the stratigraphic record. While only a limited interval of the early Pleistocene-aged WFB (~220 kyrs from ~2.21 to ~1.96 Ma) was astronomically tuned (supported by magneto-biostratigraphy), these data revealed a strong linkage between insolation paced glacio-eustasy and sediment supply (Vaucher et al., 2021). Hence, the WFB sedimentary record may represent one of the best archives to understand hydroclimatic changes that occur at the continent-ocean interface during the Plio-Pleistocene in the northwest Pacific.

2. Setting

2.1. Geological framework

Taiwan (Fig. 1A) is a tectonically active mountainous island in the northwest Pacific and is situated at the collision zone between the Philippine Sea Plate and the Eurasian Plate. Collision of the two plates commenced in the late Miocene (~6.5 Ma), which triggered lithospheric flexure of the Eurasian Plate and formation of the WFB (Covey, 1984; Yu and Chou, 2001; Chou and Yu, 2002; Lin and Watts, 2002; Castelltort et al., 2011). The fill of the WFB begins with the late Miocene–early Pliocene Kueichulin Formation (Fm), which is sandstone-dominated and was deposited under wave and tidal action mainly in shallow-marine and deltaic environments (Fig. 1B, C) (Castelltort et al., 2011; Nagel et al., 2013; Dashtgard et al., 2020; Dashtgard et al., 2021). The Kueichulin Fm is overlain by the late Pliocene Chinshui Shale, the latter of which is a mudstone-prone interval deposited in an offshore environment during a period of maximum flooding and increased subsidence in the WFB (Fig. 1B, D) (Castelltort et al., 2011; Nagel et al., 2013; Pan et al., 2015). The early Pleistocene Cholan Fm comprises mainly heterolithic strata deposited in shallow-marine environments and under the influence of wave, river and tidal processes (Fig. 1B, E) (Covey, 1984; Nagel et al., 2013; Pan et al., 2015; Vaucher et al., 2021). The whole interval is capped by the late Pleistocene Toukoshan Fm, which is a conglomerate-dominated interval that records deposition mainly in terrestrial environments. The shallowing-upwards Chinshui–Cholan–Toukoshan succession records infilling of the WFB associated with the westward migration of the Taiwan orogen (Fig. 1B) (Nagel et al., 2018).

2.2. Climate and sediment flux

Taiwan is situated along the path of most of the TCs generated in the northwest Pacific (Rohde, 2006) and where the East Asian Summer Monsoon (EASM) is very active (Chen and Wang, 2008; Tung et al., 2020). Taiwan is impacted by more than three TCs per year, and more than two Super-Typhoons (i.e., category 4–5 on the Saffir-Simpson Hurricane Intensity Scale; Kelman, 2013) every 10 years with evidence of past TCs preserved in the stratigraphic record of the WFB (e.g., Dashtgard et al., 2020; Dashtgard et al., 2021). Precipitation over Taiwan is evenly distributed between the EASM and TCs (Chen and Wang, 2008; Chen et al., 2010), yet >75% of sediment delivered to the Taiwan Strait occurs during TCs (Dadson et al., 2003; Dadson et al., 2005; Milliman et al., 2007; Chen et al., 2018b). Sediment discharge to the seas surrounding Taiwan mostly consists of mud (70–98%) (Kao et al., 2008) and is close to 400 Mt. annually (Milliman and Meade, 1983; Dadson et al., 2003). The sediment load can increase by over one order of magnitude during a TC if it coincides with EASM flows (Lee et al., 2015). The interaction of a TC and EASM flows slows the translation speed of the TC, and this can result in unusually long residence times of TCs over Taiwan and an increase in the volume of precipitation on land (Chien and Kuo, 2011; Wu et al., 2011). In Taiwan, sediment loads depend on the timing of TCs relative to earthquakes and vary for each river system. Besides, the ability of TC-driven runoff to carry massive amounts of sediment, TCs themselves are more effective agents of erosion than annual mean rainfall-runoff (Janapati et al., 2019). Over the past 60 years, the amount of sediment supplied from Taiwan to its strait has increased (Horng and Huh, 2011) following the increased frequency of intense precipitation over the island enhanced by global warming (Liu et al., 2009).

The strong and frequent seismic activity below and around Taiwan is the direct manifestation of the active collision between the Eurasian Plate and the Philippine Sea Plate (Lin, 2000). The regular earthquakes trigger landslides and supply a huge amount of material to the adjacent rivers. This large volume of sediment is exported to the ocean mainly during subsequent TCs (Dadson et al., 2004; Milliman et al., 2017; Chen et al., 2018b). The predominance of Taiwan-sourced sediments in the paleo-Taiwan Strait (i.e., the WFB) began following the emergence of the island during the early Pliocene (Hsieh et al., 2022), and remains until today (e.g., Horng and Huh, 2011); this suggests that during the late Pliocene to early Pleistocene Taiwan was the dominant sediment source to the WFB.

3. Materials and methods

3.1. Borehole data

The data used in this study are GR records published in Lin et al. (2007; see Supplementary Materials) which were acquired from two boreholes drilled in the WFB, Taiwan (TCDP-A: 120.73916°E, 24.20083°N, and HYS-1: 120.702024°E, 24.399908°N; Fig. 1A, F). Gamma-ray data are given in API (American Petroleum Institute) units with higher values being typical of mudstone-dominated strata which are normally enriched in uranium, thorium, and potassium-bearing minerals (e.g., Schlumberger, 1989). Conversely, lower GR values are typical of sandstone-dominated strata. A comparison of stratigraphic logs derived from core to GR records indicates that in general, mudstone is recorded by GR values higher than 105 API, heterolithic intervals (interbedded sandstone and mudstone) have values between 75 and 105 API, and sandstone is lower than 75 API. Because GR logs robustly trace mudstone variability in the strata (Schlumberger, 1989) they can be linked to paleoenvironmental and paleoclimatic condition changes (Worthington, 1990; Baumgarten et al., 2015; Du et al., 2020; Read et al., 2020; Ulfers et al., 2021; Cao et al., 2022; Sinnesael et al., 2022; Ulfers et al., 2022).

The stratigraphy in the two studied boreholes comprises (from base to top), the upper part of Kueichulin Fm, the Chinshui Shale, and the lower part of the Cholan Fm (see Lin et al., 2007). Formation boundaries were defined as follows: i) the Kueichulin Fm is sandstone-dominated and differs from the Cholan Fm by the absence of thick mudstone intervals, ii) the Chinshui Shale is recognized by large intervals (several tens of meters) of mudstone and by the absence of thick sandstone beds; and iii) the Cholan Fm is defined by thick (up to 70 m), quasi-cyclic intervals that comprise up to 10 m thick mudstone packages overlain by thick sandstone with limited bioturbation. In the GR record from well HYS-1, the Kueichulin-Chinshui and the Chinshui-Cholan limits are set at a depth of 1894 m and 1630 m, respectively (Fig. 1F). In the GR record from well TCDP-A, the Kueichulin-Chinshui and the Chinshui-Cholan limits are defined at a depth of 1300 m and 1013 m, respectively (Fig. 1F).

3.2. Stratigraphy and time series analyses

The astronomical tuning was built on the existing magneto-biostratigraphy for the WFB, which is widely applied. The Chinshui Shale is a temporally well-constrained mudstone-rich stratigraphic unit

that is used as marker in the WFB. The Chinshui Shale is clearly identified in both TCDP-A, and HYS-1 (Lin et al., 2007) and the magneto-biostratrigraphy places the Gilbert-Gauss (~3.6 Ma) and Gauss-Matuyama (~2.58 Ma) polarity boundaries close to the base and top of the formation, respectively (Fig. 1B) (Chen et al., 1977; Chen et al., 2001; Horng and Shea, 2007; Vaucher et al., 2021). Additional information and detailed correlation between TCDP-A, HYS-1 and a temporally constrained co-eval outcrop can be found in Lin et al. (2007). Based on the time control points, the GR signals were tuned to the benthic foraminifera stable oxygen isotope ($\delta^{18}O$) record from the equatorial Atlantic dataset of Wilkens et al. (2017), which includes an established astronomically tuned time scale. The $\delta^{18}O$ signal mainly represents global ice volume and deep-sea temperatures (Savin et al., 1975).

The tuning of GR data to the $\delta^{18}O$ record was applied to the GR record from HYS-1 between 1900 and 1380 m depth (Fig. 2A), and in TCDP-A between 1285 and 710 m (Fig. 2B). The tuning of the GR to the $\delta^{18}O$ record follows the arguments that mudstone-dominated intervals (high GR signals) are rich in clay minerals, and clay minerals are more likely to form and accumulate in i) warm and humid climates (e.g., Chen et al., 2020; Du et al., 2020), and ii) when sea level is high and coarse clastic material (i.e., sand) is trapped closer to the paleoshoreline (Catuneanu et al., 2011). Additionally, the Pliocene-to-Pleistocene transition records a global cooling condition associated with a relatively low sea level (e.g., Shackleton et al., 1990; Clark et al., 1999; Zachos et al., 2001), and this is represented in both GR records by a low-API (i.e., sandstone-rich interval; Fig. 2). Consequently, we tied the lowest GR signals in-phase to $\delta^{18}O$ maxima (i.e., global cold phases and sea-level minima), and high GR (i.e., clay-rich intervals) intervals to $\delta^{18}O$ minima (i.e., global warm phases and sea-level high-stands). Clay-rich intervals record times when fine clastic material is shed into more proximal positions. Finally, we also accounted for the increase in sedimentation rates upward through the Cholan Fm (Fig. 2F), which was previously mentioned in other studies (Chen et al., 1977; Chi and Huang, 1981; Vaucher et al., 2021).

To test the robustness of our tuning we assess the obliquity amplitude and its relation to orbital obliquity using the 'TestTilt' function in R. This method filters the record for obliquity, determines the obliquity amplitude, and then compares the data obliquity amplitude to the calculated obliquity index of Laskar et al. (2004). The method accounts for possible frequency modulation of the tuning process (Meyers, 2014; Zeeden et al., 2019; R Core Team, 2022). In order to assess the imprint of orbital forcing on the dataset, wavelet analysis was performed using the 'biwavelet' R package (Gouhier et al., 2021; R Core Team, 2022). In addition, Taner filters for 41-kyr and 20-kyr cycles were applied to evaluate the individual effect of obliquity and precession forcing, respectively, using the 'astrochron' R package (Meyers, 2014; R Core Team, 2022). The tie points for tunning and R script are available as Supplementary Materials.

4. Results

4.1. Age model and sedimentation

Our study focuses on the time interval covering the entire Chinshui Shale and the lower part of the Cholan Fm (Figs. 1 and 2). The tuning results of the GR dataset (Fig. 2A, B) to the $\delta^{18}O$ record (Fig. 2C) reveal that the age of the studied interval spans from ~3.15 to ~1.95 Ma (Fig. 2D–F), and this allows us to refine the ages of the previously identified formation boundaries (Lin et al., 2007). The Chinshui-Kueichulin boundary is set here at 3.2 Ma and the Cholan-Chinshui at 2.52 Ma (Fig. 2). Based on our age model from tuning (Fig. 2C–E), the sedimentation rate is calculated for shorter time intervals between the main tie points (Fig. 2F). The overall sedimentation rate decreased during deposition of the Chinshui Shale until the beginning of the Cholan Fm and then increased during the deposition of Cholan Fm (Fig. 2F). The trends in sedimentation are consistent between HYS-1 and TCDP-A.

Testing for similarity between the orbital solution and data for obliquity amplitudes (of GR data, as well as the reference data used in our study) results in similar patterns for the early Pleistocene in both HYS-1 and TCDP-A records (see Fig. S1). This confirms that our time scale and its obliquity imprint are not random, but comparable on a scale of at least several 100 ka. The dissimilarity for the late Pliocene is due to a non-dominant obliquity forcing of the record, which is required for robust results of this method (Shackleton et al., 1995; Zeeden et al., 2019).

4.2. Astronomical forcing

To assess orbital forcing trends in the dataset, we compared the tuned HYS-1 and TCDP-A records with astronomical parameters, including long- (~400 kyrs) and short-eccentricity (~100 kyrs), obliquity (~40 kyrs), and precession (~20 kyrs; Fig. 3A). Our wavelet analysis indicates that short-eccentricity, obliquity, and precession cycles were recorded in both GR datasets (Fig. 3B, C). Several intervals of the HYS-1 dataset with relatively low sedimentation rates (~3–2.8 Ma, ~2.55–2.4 Ma; Fig. 2D, F) show no variability at high frequencies in the wavelet analysis (Fig. 3B, C), which is an artefact of equally spaced sampling of the GR data in time. The absence of long-eccentricity may be due to the limited duration of the dataset. In HYS-1, short-eccentricity and precession mostly influence deposition during the late Pliocene (Fig. 3B). During the early Pleistocene, obliquity mainly influenced deposition recorded in HYS-1 and particularly from ~2.6 to ~2.45 Ma and from ~2.3 to ~2.15 Ma. Precession strongly influenced sedimentation in HYS-1 from ~2.3 to ~2.05 Ma (Fig. 3B). In TCDP-A short-eccentricity is stronger during the late Pliocene, and its influence on the record is strongest from ~3.05 to ~2.75 Ma (Fig. 3C). The lower Pleistocene record in TCDP-A is dominated by obliquity, with maxima of its influence between ~2.6 to ~2.45 Ma and from ~2.3 to ~2.1 Ma (Fig. 3C). Precession also strongly affects the lower Pleistocene-aged TCDP-A records with its maximum influence between ~2.1 and ~2.2 Ma (Fig. 3C). The time interval with the strongest precession influence observed in both HYS-1 and TCDP-A coincides with the stratigraphic interval tuned to the insolation curve (i.e., precession-dominated curve) elsewhere in the WFB (Vaucher et al., 2021). The obliquity amplitude (Fig. 3A) increases throughout the studied time interval and reach its maximum between ~2.6 to ~2.3 Ma; this also corresponds to a minimum in both eccentricity and precession (Fig. 3B, C).

5. Discussion

5.1. Stratigraphic completeness

While autogenic and/or allogenic processes may affect the completeness of the sedimentary record of shallow-marine environments (Barrell, 1917; Sadler, 1981; Paola et al., 2018), we argue that the selected study sites, HYS-1 and TCDP-A, provide a quasi-continuous record of paleoenvironmental and palaeoclimatological variability during the Plio-Pleistocene transition. Indeed, the stratigraphic record of the WFB is defined by high rates of sediment accumulation due to the fast growing orogenesis and the massive sediment supply from Taiwan (Chi and Huang, 1981; Chen et al., 2001; Lin et al., 2003; Nagel et al., 2018; Vaucher et al., 2021). Consequently, it is reasonable to assume that the net accumulation of sediment is high enough to preserve past climate oscillations at least on orbital time scales (with rates of mostly ~0.3–0.8 m/kyr) and at minimum on precession time scales (Figs. 2–4); this has been demonstrated both in the WFB for the time interval ~2.21 to ~1.96 Ma (Vaucher et al., 2021), and in relatively comparable basinal settings under similar water depths (Naish et al., 1998; Marshall et al., 2017). While we anticipate that the general trends of climate cycles variations are preserved and expressed in the stratigraphic record, we acknowledge that individual cycles might be incomplete especially in

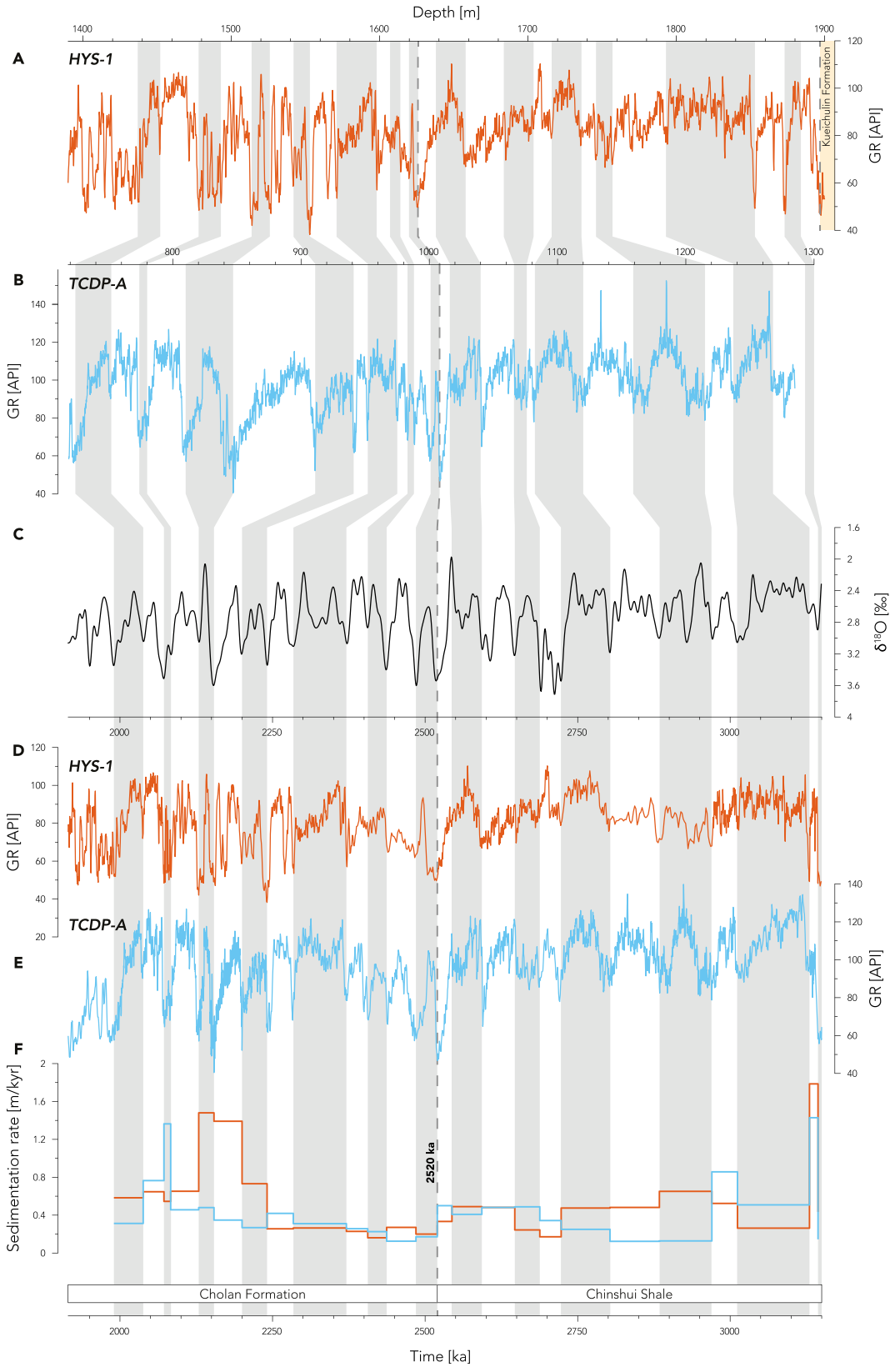

Fig. 2. Astronomical tuning. The astronomical tuning and correlation of the gamma-ray data from (A) HYS-1 and (B) TCDP-A boreholes (Lin et al., 2007) with the (C) $\delta^{18}O$ record from benthic foraminifera (Wilkens et al., 2017). The thick gray dashed line indicated the identified formation boundaries (Lin et al., 2007). The astronomically tuned GR data from (D) HYS-1 and (E) TCDP-A are use to calculate (F) sedimentation rate. Sedimentation rates are consistent between the two studied localities. They are also relatively stable throughout the deposition of the Chinshui Shale and it increases in the Cholan Formation. Astronomical tuning is use to define the Chinshui-Kuechulin boundary at ~3.2 Ma and the Cholan-Chinshui boundary at 2.52 Ma.

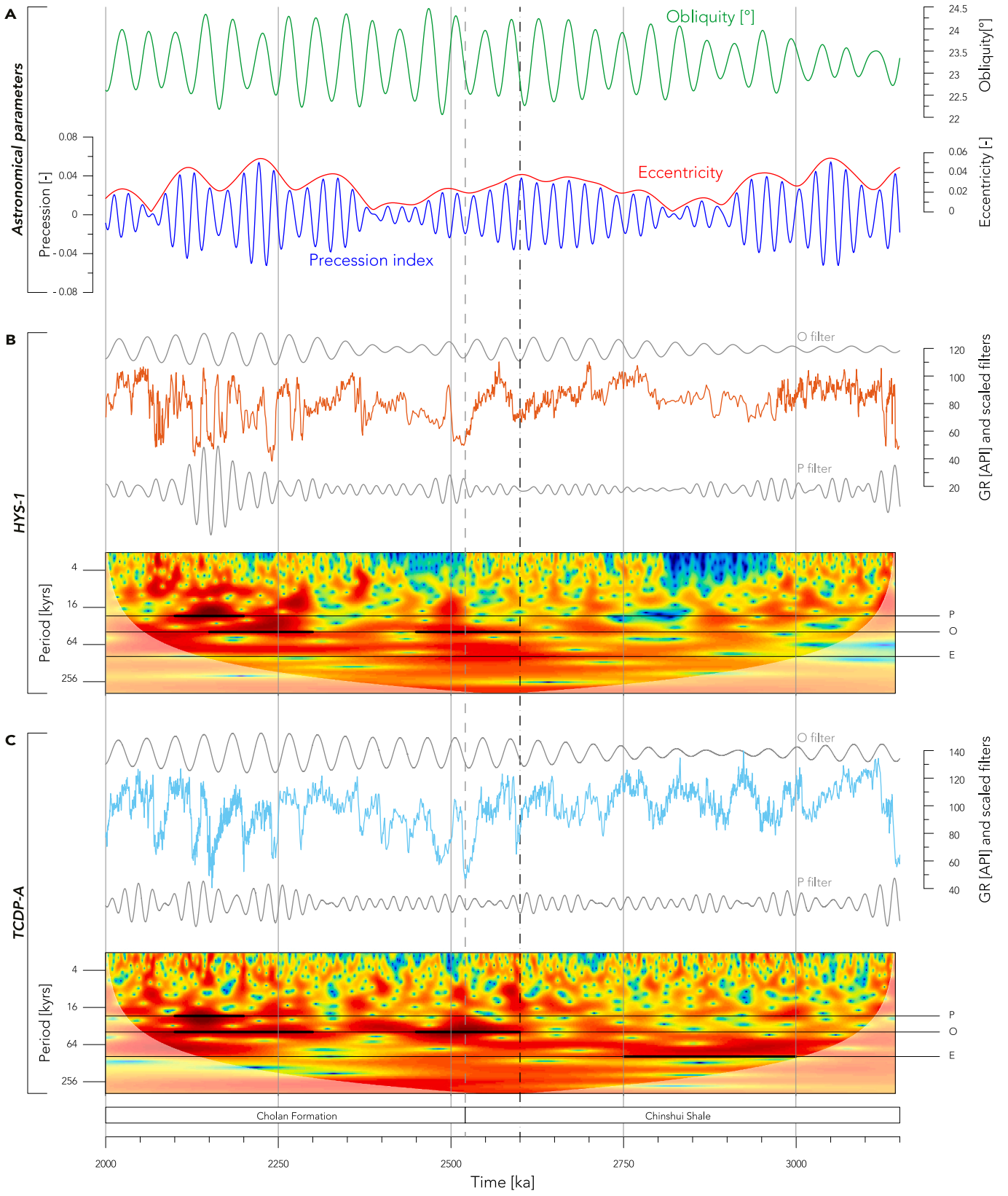

Fig. 3. Frequency analyses of the tuned dataset. (A) Astronomical solutions of the eccentricity, obliquity and precession indices for the studied time interval (Laskar et al., 2004). (B) Tuned and scaled gamma ray data from HYS-1 borehole with obliquity and precession filters, and its wavelet analysis. (C) Tuned and scaled gamma ray data from TCDP-A borehole with obliquity and precession filters, and its wavelet analysis. The thick gray dashed line indicates the boundary between the Chinshui Shale and the Cholan Formation. The dashed-dotted black line is the Pliocene-Pleistocene boundary at 2.58 Ma. Abbreviations: P: Precession; O: Obliquity; E: Eccentricity. Thick black lines on orbital periods correspond to those specifically mentioned in the text. Wavelet analysis: blue colors represent low spectral power; red represents high spectral power. (For interpretation of the references to colour in this figure legend, the reader is referred to the web version of this article.)

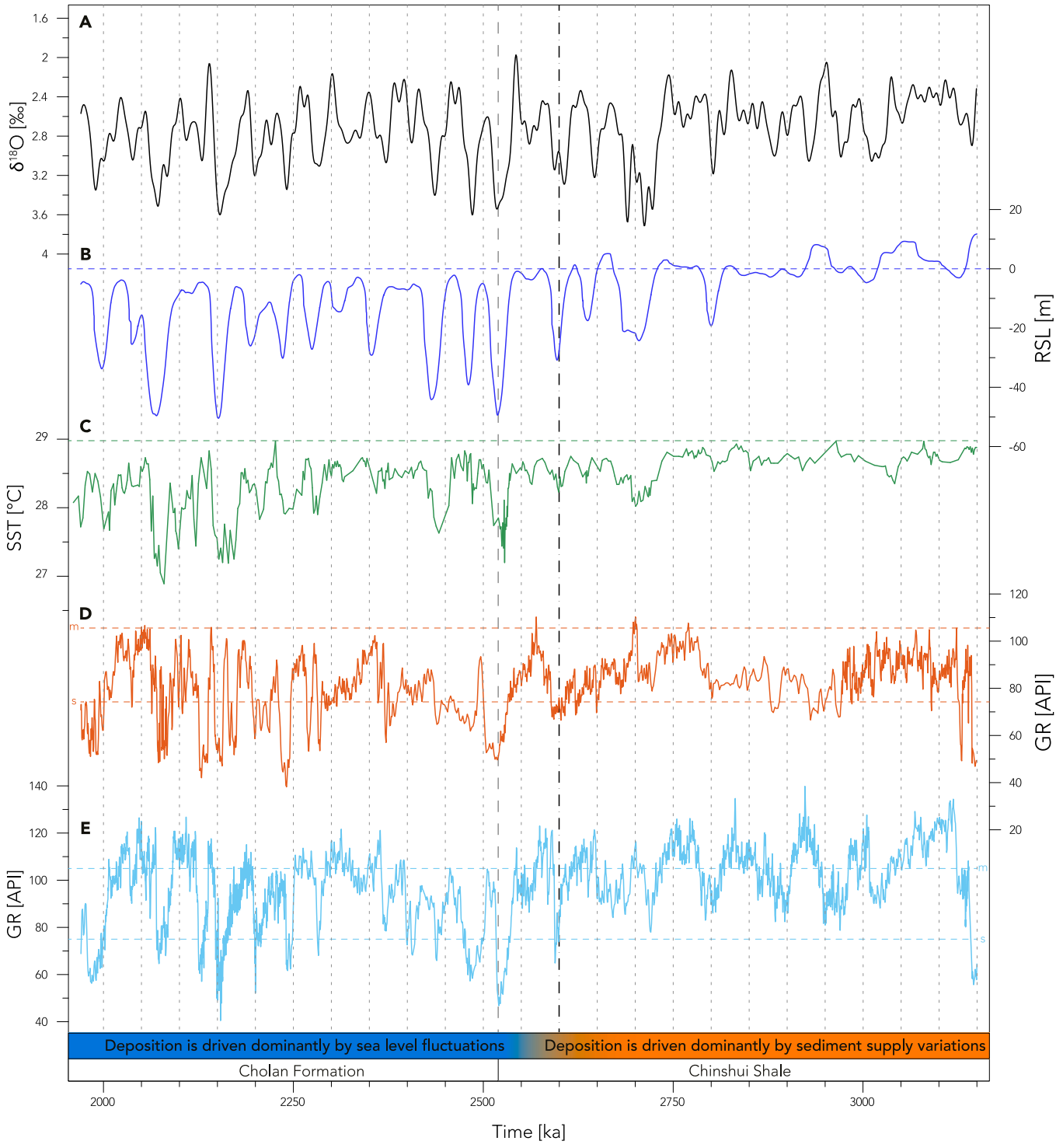

Fig. 4. Hydroclimate dynamics during the Plio-Pleistocene transition. (A) Oxygen isotope proxy data (in black) (Wilkens et al., 2017), (B) relative sea level (RSL; in dark blue) reconstruction (Berends et al., 2021), and (C) alkenone based sea-surface temperature (SST; in green) from the South China Sea (Li et al., 2011) are compared to the tuned gamma ray datasets from (D) HYS-1 (in orange) and (E) TCDP-A (in light blue) boreholes. The interval covers the late Pliocene to early Pleistocene and spans from 3.15 to 1.95 Ma. The thick gray dashed line indicates the identified formation boundary. The dashed-dotted black line represents the Pliocene-Pleistocene boundary set at 2.58 Ma. The dark blue dashed line highlights (B) the present-day value sea level (0 m). The green dashed line (C) corresponds to the temperature of 28.97 °C (Uk'37 = 1.0). The orange and light blue dashed lines in (D) and (E), respectively, indicate the GR limits for sandstone (s; < 75 API) and mudstone (m; > 105 API). (For interpretation of the references to colour in this figure legend, the reader is referred to the web version of this article.)

sandstone (i.e., low GR) intervals. Nevertheless, the completeness of the stratigraphic record herein is supported by i) the similarity in trends between the benthic $\delta^{18}O$ record (used as a tuning target) and the GR records from both studied intervals (Figs. 2 and 4), and ii) the robustness of the generated time scale and its orbital imprint (Fig. 3 and S1). Based on this, we propose that the shallow-marine stratigraphic record in the WFB preserves an exceptional late Cenozoic climate record.

5.2. Hydroclimate dynamics

5.2.1. The late Pliocene

During the late Pliocene (from 3.15 to 2.58 Ma; Fig. 4), both global sea level and sea-surface temperatures in the northwest Pacific show relatively limited change suggesting rather stable and warm climate conditions (Fig. 4B, C) (Li et al., 2011; Berends et al., 2021). At the same time, the GR records of HYS-1 and TCDP-A both show fluctuations (Fig. 4D, E) that correlate closely to the short-eccentricity and precession frequency bands (Fig. 3B, C). High GR responses mark muddier stratigraphic intervals and by assumption, correlate to warmer climate conditions (Figs. 3B, C and 4D, E). During the late Pliocene, the global sea level and sea-surface temperatures in the northwest Pacific show limited variability (Fig. 4B, C), while both tuned GR datasets depicted high-frequency cyclic changes (Fig. 4 D, E).

The thick interval of fine-grained sediments (i.e., mudstone-rich) deposited in the WFB during the late Pliocene is typical for most offshore environments (e.g., Catuneanu et al., 2009; MacEachern et al., 2012). However, cyclic sandier intervals in the offshore could reflect either shoreline progradation (and associated sediment bypass into deeper water) or changes in the nature of sediment exported from land to sea (e.g., Burgess and Prince, 2015). Four parameters must be considered in determining whether sea level or sediment supply is the main driver of the observed finer-to-coarser depositional cycles during the late Pliocene Chinshui Shale. First, paleoenvironmental reconstructions of the Chinshui Shale suggest that sea level was relatively high and stable throughout its deposition, and water depths estimated for the studied locations are $\geq$35 m without evidence of significant shoreline migration (Nagel et al., 2013). Second, the land-to-ocean sediment transfer from Taiwan during the late Pliocene was comparable to present-day conditions (Dashtgard et al., 2021; Hsieh et al., 2022; Huang et al., 2022; Nayak et al., 2022). Third, a higher flux of sediment correlated to the increased frequency of intense rainfall over the past decades is monitored in the Taiwan Strait and is likely due to increasing temperature (Liu et al., 2009; Horng and Huh, 2011). Fourth, the EASM is mainly driven by changes in low-latitude insolation controlled by changes in eccentricity-modulated precession (Gai et al., 2020; Liu et al., 2021). Taking into consideration the current climatic conditions affecting Taiwan, we suggest that the finer-to-coarser depositional cycles preserved in our GR dataset relate mostly to the interactions between EASM strength and TC activity recorded in offshore settings during the studied time interval and probably do not reflect solely sea-level fluctuations. The interactions between the EASM and TCs varied in intensity via orbital forcing and drove changes in the type and volume of sediment exported from Taiwan into the paleo-Taiwan Strait (i.e., the WFB).

We posit that the finest grained sediment deposited during the late Pliocene is linked to enhanced EASM and TC activity. Increased EASM and TC activity was probably due to the El Niño conditions that prevailed at that time (Camargo et al., 2007; Zhang et al., 2018; Shao et al., 2020; Kaboth-Bahr and Mudelsee, 2022), which resulted in increased erosion of rapidly uplifting and poorly-consolidated mudstone; these sediments were subsequently exported into offshore environments. Additionally, the positive feedback of TC activities enhancing El Niño conditions (Wang et al., 2019) might have reinforced the impacts of the EASM. Despite periods of weaker EASM in the late Pliocene, temperatures in the northwest Pacific remain above the threshold limit for the formation of TCs (26.5–27.0 °C; Fig. 4C) (Tory and Frank, 2012). After relatively protracted periods of intense EASM-TC activity, probably most of the fine-grained material available in river catchments (dominantly clay-rich sediment) was exported into the adjacent seas. Enhanced runoff during peaks of the EASM-TC is also supported by the fact that deposited muddier intervals are always thicker than sandier intervals (Fig. 2A, B). This repeated massive export of mud from the hinterland into offshore environments of the paleo-Taiwan Strait could be similar to periods subject to frequent *system-clearing* events (Jerolmack and Paola, 2010), the latter of which are also recorded in natural systems during catastrophic floods occurring over several thousand years (Chen et al., 2018a). Even if we cannot entirely exclude small amplitude sea-level fluctuations to explain some sandier (and potentially shallower) intervals (e.g., at ~2.7 and ~2.8 Ma; Fig. 4), we propose that sandier intervals correspond to cooler periods during which the *recovery phase* of Taiwanese watersheds occurred. In addition, during relatively cooler periods, the climate becomes drier, and vegetation might have been reduced, promoting physical erosion of bedrock in the hinterland of Taiwan. Consequently, sandier sediment becomes more available in the watersheds to be exported by TCs during periods of weaker EASM, and these eroded sands were deposited in offshore environments.

5.2.2. The early Pleistocene

During the early Pleistocene (from 2.58 to 1.95 Ma; Fig. 4), global sea level and regional sea-surface temperatures were significantly more variable than during the late Pliocene (Fig. 4B, C). At the same time, Taiwan's westward migration continued, which is expressed by the shallower depositional environments of the Cholan Fm compared to the Chinshui Shale (Fig. 1B, C). Eustatic sea-level variations during the early Pleistocene show amplitudes of 25–50 m (Fig. 4B) (Berends et al., 2021), and sea-surface temperatures in the northwest Pacific fluctuated between 26 °C and 29 °C but with an overall decreasing trend (Fig. 4C) (Li et al., 2011). The two GR datasets also present similar trends to those depicted by sea level and sea-surface temperatures (Fig. 4D, E), suggesting that uplift and westward migration of the Taiwan orogen did not significantly affect the preservation of climate signals. The variability in GR responses in HYS-1 and TCDP-A correlate dominantly to obliquity and precession cycles in the upper Chinshui Shale–lower Cholan Fm and between ~2.7 and ~1.95 Ma (Fig. 3B, C). Towards the Plio-Pleistocene boundary, sandstone intervals become more pronounced than during the late Pliocene. This could mean more intense EASM and TC activity; however, the general cooling trend at the time (Shackleton et al., 1990; Clark et al., 1999) alongside the shift towards more permanent La Niña conditions in the northwest Pacific (Kaboth-Bahr and Mudelsee, 2022) does not support this as TCs were weaker in intensity (Camargo et al., 2007). Alternatively, the intensification of the ice-sheet cover in the Northern Hemisphere and its related glacial cycles are more likely to have driven sandstone deposition during periods of low sea level.

Between ~2.6 and ~2.3 Ma, the precession/eccentricity cyclicity decreases towards its weakest amplitude while obliquity shows a higher amplitude (Fig. 3A). Such a scenario is reflected in both GR datasets with a dominant obliquity signal during this time interval (red colors at ~40 kyr period in Fig. 3B, C). We note that the average calculated sedimentation rate is higher from 3.15 to 2.6 Ma and from 2.3 to 2.1 Ma (Fig. 2F) than it is from 2.6 to 2.3 Ma, the latter of which coincides with the obliquity maxima (Figs. 3 and S1). The decrease in the eccentricity/precession signal amplitude between 2.6 and 2.3 Ma would have reduced low-latitude insolation which would lower EASM and TC activities. In turn, lower EASM and TC activity would decrease the sediment supply resulting in a reduced sedimentation rate (Fig. 2F). While low-latitude forcing driven by eccentricity-modulated precession is weakened between 2.6 and 2.3 Ma, this condition allowed for an increasing influence of obliquity forcing on the system. Still, it remains unclear whether obliquity drove high- or low-latitude forcing. Obliquity is responsible mainly for modulation of insolation received at high latitudes and resulting from the growth and decay of ice sheets; this leads to quasi-cyclic sea-level fluctuations (Milankovitch, 1941; Shackleton, 1967; Hays et al., 1976). However, obliquity fluctuation can directly affect low-latitude climate without high-latitude ice sheet fluctuations solely by changes in the cross-equatorial insolation gradient (Bosmans et al., 2015; Liu et al., 2015). While we cannot exclude a low-latitude obliquity influence on the studied interval, the lower Pleistocene Cholan Fm, which was deposited at water depths between ~50 and ~15 m, shows multiple periods of shoreline migration (Covey, 1984; Chen

et al., 2001; Nagel et al., 2013; Pan et al., 2015; Vaucher et al., 2021). Therefore, the hypothesis of obliquity-induced ice-sheets fluctuation (i.e., high latitude climate forcing) is preferred.

Sea-surface temperature and sea-level reconstructions show the same trend of "cooling and sea-level drop" during the early Pleistocene (Fig. 4). These fluctuations probably result from the development of the Northern Hemisphere ice sheets (Shackleton et al., 1990; Clark et al., 1999) with glacial-interglacial periods that translate into quasi-cyclic sea-level fluctuations (Milankovitch, 1941; Shackleton, 1967; Hays et al., 1976). These cycles are commonly interpreted during the early Pleistocene (based on the 41-kyr duration of cycles depicted by foraminiferal $\delta^{18}O$) to be driven by Earth's obliquity (Raymo and Nisancioglu, 2003; Lisiecki and Raymo, 2005; Huybers, 2006; Raymo et al., 2006; Lisiecki and Raymo, 2007; Tabor et al., 2015). However, this interpretation has been challenged recently by additional evidence of considerable precession contribution to glacial-interglacial cycles induced by variations in summer insolation received in the Northern Hemisphere (Liautaud et al., 2020; Vaucher et al., 2021; Barker et al., 2022). Given the orbital forcing (Figs. 3 and 4), we propose that the fluctuations observed in both GR datasets between ~2.6 and ~2.3 Ma reflect mainly obliquity-dominated sea-level changes and the variations observed in the GR values between ~2.3 and ~1.95 Ma probably record sea-level variations paced by precession. The dominance of precession signals was demonstrated previously in coeval strata in the WFB albeit for a shorter interval (Vaucher et al., 2021). In turn, the absence of precession-paced sea level in the global sea-level reconstruction (Fig. 4B) is potentially caused by these being based mainly on $\delta^{18}O$ of benthic foraminifera from deep sea settings (Berends et al., 2021).

6. Conclusion

We analyzed gamma-ray data from two boreholes through shallow-marine strata of the Western Foreland Basin, Taiwan. The gamma-ray records span from ~3.15 to ~1.95 Ma, and from these data we assess hydroclimate dynamics in the northwest Pacific. Our study indicates that the late Pliocene stratigraphic record is probably dominated by a complex interaction between the East Asian Summer Monsoon and tropical cyclones, which were forced mainly by low-latitude insolation in response to eccentricity-modulated precession. This low-latitude climate forcing led to a period of massive export and deposition of mudstone in the basin, which was punctuated by recovery phases of Taiwanese watersheds. The early Pleistocene record is dominated by sea-level fluctuations driven by glacial-interglacial cycles (high-latitude climate forcing), which are mainly paced by obliquity (~2.6 to ~2.3 Ma) and then precession (~2.3 to ~1.95 Ma). The Plio-Pleistocene shallow-marine strata of the Western Foreland Basin allow for the differentiation between high- and low-latitude climate forcing in the northwest Pacific and reveal a more complex story of past hydroclimate dynamics that traditional climate archives typically capture.

Author contributions

R.V. and C.Z. designed the study, interpreted the data, and drew the figs. C.Z. perform the statistical analysis. R.V., C.Z., A.I.H., S.K-B., C-S. H., S.E.D. discussed the data. A.T.L. provided the raw data from the boreholes. R.V. wrote the manuscript with inputs from all co-authors. All co-authors reviewed and approved the manuscript.

Declaration of Competing Interest

The authors declare no conflict of interest.

Data availability

All data needed supporting the conclusions of this study are present within the article and Supplementary Materials. Additional data related to this paper may be requested from the authors

Acknowledgments

R.V. research was supported through Swiss National Science Foundation grants (P400P2_183946 and P5R5PN_202846). S.K.-B. acknowledges funding from an Open-Topic Post-Doc fellowship of the University of Potsdam, the Deutsche Forschungsgemeinschaft (DFG) grant number KA 4757/3-1, and from the German Academic Exchange Service (DAAD) under grant number 57558354 and 57603159. R.V., C.Z., A.I.H., and S. E.D. also received funding through Deutsche Forschungsgemeinschaft (DFG) project number 456312283. We appreciate the constructive feedback from two anonymous reviewers and Editor Dr. Alan Haywood who helped improving the quality of the manuscript.

Appendix A. Supplementary data

Supplementary data to this article can be found online at https://doi.org/10.1016/j.gloplacha.2023.104088.

References

Barker, S., Starr, A., Lubbe, J.V.D., Doughty, A., Knorr, G., Conn, S., Lordsmith, S., Owen, L., Nederbragt, A., Hemming, S., Hall, I., Levay, L., Berke, M.A., Brentegani, L., Caley, T., Cartagena-Sierra, A., Charles, C.D., Coenen, J.J., Crespin, J. G., Franzese, A.M., Gruetzner, J., Han, X., Hines, S.K.V., Espejo, F.J.J., Just, J., Koutsodendris, A., Kubota, K., Lathika, N., Norris, R.D., Santos, T.P.D., Robinson, R., Rolison, J.M., Simon, M.H., Tangunan, D., Yamane, M., Zhang, H., 2022. Persistent influence of precession on northern ice sheet variability since the early Pleistocene. Science 376, 961–967. https://doi.org/10.1126/science.abm4033.

Barrell, J., 1917. Rhythms and the measurements of geologic time. GSA Bull. 28, 745–904. https://doi.org/10.1130/gsab-28-745.

Baumgarten, H., Wonik, T., Tanner, D.C., Francke, A., Wagner, B., Zanchetta, G., Sulpizio, R., Giaccio, B., Nomade, S., 2015. Age–depth model of the past 630 kyr for Lake Ohrid (FYROM/Albania) based on cyclostratigraphic analysis of downhole gamma ray data. Biogeosciences 12, 7453–7465. https://doi.org/10.5194/bg-12-7453-2015.

Beaufort, L., Bolton, C.T., Sarr, A.C., Sucheras-Marx, B., Rosenthal, Y., Donnadieu, Y., Barbarin, N., Bova, S., Cornuault, P., Gally, Y., Gray, E., Mazur, J.C., Tetard, M., 2022. Cyclic evolution of phytoplankton forced by changes in tropical seasonality. Nature 601, 79–84. https://doi.org/10.1038/s41586-021-04195-7.

Berends, C.J., de Boer, B., Dolan, A.M., Hill, D.J., van de Wal, R.S.W., 2019. Modelling ice sheet evolution and atmospheric CO2 during the late Pliocene. Clim. Past 15, 1603–1619. https://doi.org/10.5194/cp-15-1603-2019.

Berends, C.J., de Boer, B., van de Wal, R.S.W., 2021. Reconstructing the evolution of ice sheets, sea level, and atmospheric CO2 during the past 3.6 million years. Clim. Past 17, 361–377. https://doi.org/10.5194/cp-17-361-2021.

Bosmans, J.H.C., Hilgen, F.J., Tuenter, E., Lourens, L.J., 2015. Obliquity forcing of low-latitude climate. Clim. Past 11, 1335–1346. https://doi.org/10.5194/cp-11-1335-2015.

Burgess, P.M., Prince, G.D., 2015. Non-unique stratal geometries: implications for sequence stratigraphic interpretations. Basin Res. 27, 351–365. https://doi.org/10.1111/bre.12082.

Burke, K.D., Williams, J.W., Chandler, M.A., Haywood, A.M., Lunt, D.J., Otto-Bliesner, B. L., 2018. Pliocene and Eocene provide best analogs for near-future climates. Proc. Natl. Acad. Sci. 115, 13288–13293. https://doi.org/10.1073/pnas.1809600115.

Camargo, S.J., Robertson, A.W., Gaffney, S.J., Smyth, P., Ghil, M., 2007. Cluster Analysis of Typhoon Tracks. Part II: Large-Scale Circulation and ENSO. J. Clim. 20, 3654–3676. https://doi.org/10.1175/jcli4203.1.

Cao, H., Jin, S., Hou, M., Chen, S., Liu, Y., Chen, A., 2022. Astronomical cycles calibrated the sea-level sequence durations of late Miocene to Pliocene in Qiongdongnan Basin, South China Sea. Mar. Pet. Geol. 105813 https://doi.org/10.1016/j.marpetgeo.2022.105813.

Castelltort, S., Nagel, S., Mouthereau, F., Lin, A.T.-S., Wetzel, A., Kaus, B., Willett, S., Chiang, S.-P., Chiu, W.-Y., 2011. Sedimentology of early Pliocene sandstones in the South-Western Taiwan foreland: Implications for basin physiography in the early stages of collision. J. Asian Earth Sci. 40, 52–71. https://doi.org/10.1016/j.jseaes.2010.09.005.

Catuneanu, O., Abreu, V., Bhattacharya, J.P., Blum, M.D., Dalrymple, R.W., Eriksson, P. G., Fielding, C.R., Fisher, W.L., Galloway, W.E., Gibling, M.R., Giles, K.A., Holbrook, J.M., Jordan, R., Kendall, C.G.S.C., Macurda, B., Martinsen, O.J., Miall, A. D., Neal, J.E., Nummedal, D., Pomar, L., Posamentier, H.W., Pratt, B.R., Sarg, J.F., Shanley, K.W., Steel, R.J., Strasser, A., Tucker, M.E., Winker, C., 2009. Towards the standardization of sequence stratigraphy. Earth Sci. Rev. 92, 1–33. https://doi.org/10.1016/j.earscirev.2008.10.003.

Catuneanu, O., Galloway, W.E., Kendall, C.G.S.C., Miall, A.D., Posamentier, H.W., Strasser, A., Tucker, M.E., 2011. Sequence Stratigraphy: Methodology and nomenclature. Newsl. Stratigr. 44, 173–245. https://doi.org/10.1127/0078-0421/2011/0011.

Chen, T.-C., Wang, S.-Y., 2008. Measuring East Asian Summer Monsoon Rainfall Contributions by Different Weather Systems over Taiwan. J. Appl. Meteorol. Climatol. 47, 2068–2080. https://doi.org/10.1175/2007jamc1821.1.
Chen, P.-H., Huang, T.-C., Huang, C.-Y., Jiang, M.-J., Lo, S.-L., Kuo, C.-L., 1977. Paleomagnetic and coccolith stratigraphy of Plio-Pleistocene shallow marine sediments, Chuhuangkeng, Miaoli. Pet. Geol. Taiwan 14, 219–239.
Chen, W.-S., Ridgway, K.D., Horng, C.-S., Chen, Y.-G., Shea, K.-S., Yeh, M.-G., 2001. Stratigraphic architecture, magnetostratigraphy, and incised-valley systems of the Pliocene-Pleistocene collisional marine foreland basin of Taiwan. GSA Bull. 113, 1249–1271. https://doi.org/10.1130/0016-7606(2001)113<1249:SAMAIV>2.0.CO;2.
Chen, J.-M., Li, T., Shih, C.-F., 2010. Tropical Cyclone– and Monsoon-Induced Rainfall Variability in Taiwan. J. Clim. 23, 4107–4120. https://doi.org/10.1175/2010JCLI3355.1.
Chen, C., Guerit, L., Foreman, B.Z., Hassenruck-Gudipati, H.J., Adatte, T., Honegger, L., Perret, M., Sluijs, A., Castelltort, S., 2018a. Estimating regional flood discharge during Palaeocene-Eocene global warming. Sci. Rep. 8, 13391. https://doi.org/10.1038/s41598-018-31076-3.
Chen, C.-W., Oguchi, T., Hayakawa, Y.S., Saito, H., Chen, H., Lin, G.-W., Wei, L.-W., Chao, Y.-C., 2018b. Sediment yield during typhoon events in relation to landslides, rainfall, and catchment areas in Taiwan. Geomorphology 303, 540–548. https://doi.org/10.1016/j.geomorph.2017.11.007.
Chen, G., Gang, W., Tang, H., Gao, G., Wang, N., Liu, L., Yang, S., Wang, Y., 2020. Astronomical cycles and variations in sediment accumulation rate of the terrestrial lower cretaceous Xiagou Formation from the Jiuquan Basin, NW China. In: Cretaceous Research, 109. https://doi.org/10.1016/j.cretres.2019.06.002.
Chi, W.-R., Huang, H.-M., 1981. Nannobiostratigraphy and paleoenvironments of the late Neogene sediments and their tectonic implications in the Miaoli area, Taiwan. Pet. Geol. Taiwan 18, 111–129.
Chien, F.-C., Kuo, H.-C., 2011. On the extreme rainfall of Typhoon Morakot (2009). J. Geophys. Res.-Atmos. 116 https://doi.org/10.1029/2010JD015092.
Chou, Y.-W., Yu, H.-S., 2002. Structural Expressions of Flexural Extension in the Arc-Continent Collisional Foredeep of Western Taiwan, Geology and Geophysics of an Arc-Continent Collision. Geological Society of America, Taiwan, p. 0.
Clark, P.U., Alley, R.B., Pollard, D., 1999. Northern Hemisphere Ice-Sheet Influences on Global climate Change. Science 286, 1104–1111. https://doi.org/10.1126/science.286.5442.1104.
Cohen, K.M., Gibbard, P.L., 2019. Global chronostratigraphical correlation table for the last 2.7 million years, version 2019 QI-500. Quat. Int. 500, 20–31. https://doi.org/10.1016/j.quaint.2019.03.009.
Coumou, D., Rahmstorf, S., 2012. A decade of weather extremes. Nat. Clim. Chang. 2, 491. https://doi.org/10.1038/nclimate1452.
Covey, M., 1984. Lithofacies analysis and basin reconstruction, Plio-Pleistocene Western Taiwan Foredeep. Pet. Geol. Taiwan 20, 53–83.
Dadson, S.J., Hovius, N., Chen, H., Dade, W.B., Hsieh, M.-L., Willett, S.D., Hu, J.-C., Horng, M.-J., Chen, M.-C., Stark, C.P., Lague, D., Lin, J.-C., 2003. Links between erosion, runoff variability and seismicity in the Taiwan orogen. Nature 426, 648. https://doi.org/10.1038/nature02150.
Dadson, S.J., Hovius, N., Chen, H., Dade, W.B., Lin, J.-C., Hsu, M.-L., Lin, C.-W., Horng, M.-J., Chen, T.-C., Milliman, J., Stark, C.P., 2004. Earthquake-triggered increase in sediment delivery from an active mountain belt. Geology 32, 733–736. https://doi.org/10.1130/G20639.1.
Dadson, S., Hovius, N., Pegg, S., Dade, W.B., Horng, M.J., Chen, H., 2005. Hyperpycnal river flows from an active mountain belt. J. Geophys. Res. Earth Surf. 110 https://doi.org/10.1029/2004jf000244.
Dashtgard, S.E., Löwemark, L., Vaucher, R., Pan, Y.-Y., Pilarczyk, J.E., Castelltort, S., 2020. Tropical cyclone deposits in the Pliocene Taiwan Strait: Processes, examples, and conceptual model. Sediment. Geol. 405, 105687 https://doi.org/10.1016/j.sedgeo.2020.105687.
Dashtgard, S.E., Löwemark, L., Wang, P.-L., Setiaji, R.A., Vaucher, R., 2021. Geochemical evidence of tropical cyclone controls on shallow-marine sedimentation (Pliocene, Taiwan). Geology 49, 566–570. https://doi.org/10.1130/g48586.1.
Drury, A.J., Liebrand, D., Westerhold, T., Beddow, H.M., Hodell, D.A., Rohlfs, N., Wilkens, R.H., Lyle, M., Bell, D.B., Kroon, D., Pälike, H., Lourens, L.J., 2021. Climate, cryosphere and carbon cycle controls on Southeast Atlantic orbital-scale carbonate deposition since the Oligocene (30–0 Ma). Clim. Past 17, 2091–2117. https://doi.org/10.5194/cp-17-2091-2021.
Du, W., Ji, Y., Chen, G., Wu, H., Gao, C., Li, S., Zhang, Y., 2020. Cyclostratigraphy and astronomical tuning during the Oligocene in the Jizhong Depression, Bohai Bay Basin, northeastern China. Palaeogeogr. Palaeoclimatol. Palaeoecol. 554 https://doi.org/10.1016/j.palaeo.2020.109803.
Gai, C., Liu, Q., Roberts, A.P., Chou, Y., Zhao, X., Jiang, Z., Liu, J., 2020. East Asian monsoon evolution since the late Miocene from the South China Sea. Earth Planet. Sci. Lett. 530, 115960 https://doi.org/10.1016/j.epsl.2019.115960.
Gouhier, T.C., Grinsted, A., Simko, V., 2021. R Package Biwavelet: Conduct Univariate and Bivariate Wavelet Analyses. (Version 0.20.21). https://github.com/tgouhier/biwavelet.
Grant, K.M., Rohling, E.J., Ramsey, C.B., Cheng, H., Edwards, R.L., Florindo, F., Heslop, D., Marra, F., Roberts, A.P., Tamisiea, M.E., Williams, F., 2014. Sea-level variability over five glacial cycles. Nat. Commun. 5, 5076. https://doi.org/10.1038/ncomms6076.
Green, A.N., Cooper, J.A.G., Loureiro, C., Dixon, S., Hahn, A., Zabel, M., 2022. Stormier mid-Holocene Southwest Indian Ocean due to poleward trending tropical cyclones. Nat. Geosci. 15, 60–66. https://doi.org/10.1038/s41561-021-00842-w.
Hays, J.D., Imbrie, J., Shackleton, N.J., 1976. Variations in the Earth's Orbit: Pacemaker of the Ice Ages. Science 194, 1121–1132. https://doi.org/10.1126/science.194.4270.1121.
Haywood, A.M., Hill, D.J., Dolan, A.M., Otto-Bliesner, B.L., Bragg, F., Chan, W.L., Chandler, M.A., Contoux, C., Dowsett, H.J., Jost, A., Kamae, Y., Lohmann, G., Lunt, D.J., Abe-Ouchi, A., Pickering, S.J., Ramstein, G., Rosenbloom, N.A., Salzmann, U., Sohl, L., Stepanek, C., Ueda, H., Yan, Q., Zhang, Z., 2013. Large-scale features of Pliocene climate: results from the Pliocene Model Intercomparison Project. Clim. Past 9, 191–209. https://doi.org/10.5194/cp-9-191-2013.
Horng, C.-S., Huh, C.-A., 2011. Magnetic properties as tracers for source-to-sink dispersal of sediments: a case study in the Taiwan Strait. Earth Planet. Sci. Lett. 309, 141–152. https://doi.org/10.1016/j.epsl.2011.07.002.
Horng, C.-S., Shea, K.-S., 2007. The Quaternary Magnetobiostratigraphy of Taiwan and Penglai Orogenic Events, 18. Special Publication of the Central Geological Survey, pp. 51–83.
Hsieh, A.I., Dashtgard, S.E., Wang, P.L., Horng, C.S., Su, C.C., Lin, A.T., Vaucher, R., Löwemark, L., 2022. Multi-proxy evidence for rapidly shifting sediment sources to the Taiwan Western Foreland Basin at the Miocene–Pliocene transition. Basin Res. https://doi.org/10.1111/bre.12741.
Huang, S.-Y., Lee, Y.-H., Mesalles, L., Horng, C.-S., Lu, H.-Y., Tsai, Y.-L., Wu, Y.-J., Chen, F.-Y., Tan, X.-B., 2022. Plio-Pleistocene fluvial dynamics in the pro-foreland basins of Taiwan: Thermochronological constraints and tectonic implications from the syn-orogenic deposits. Tectonophysics 838, 229486. https://doi.org/10.1016/j.tecto.2022.229486.
Huybers, P., 2006. Early Pleistocene Glacial Cycles and the Integrated Summer Insolation Forcing. Science 313, 508–511. https://doi.org/10.1126/science.1125249.
IPCC, 2021. In: Masson-Delmotte, V., et al. (Eds.), Climate Change 2021: The Physical Science Basis. Contribution of Working Group I to the Sixth Assessment Report of the Intergovernmental Panel on Climate Change. Cambridge University Press.
Janapati, J., Seela, B.K., Lin, P.-L., Wang, P.K., Kumar, U., 2019. An assessment of tropical cyclones rainfall erosivity for Taiwan. Sci. Rep. 9, 15862. https://doi.org/10.1038/s41598-019-52028-5.
Jerolmack, D.J., Paola, C., 2010. Shredding of environmental signals by sediment transport. Geophys. Res. Lett. 37 https://doi.org/10.1029/2010gl044638 n/a-n/a.
Jerolmack, D.J., Sadler, P., 2007. Transience and persistence in the depositional record of continental margins. J. Geophys. Res. 112 https://doi.org/10.1029/2006jf000555.
Kaboth-Bahr, S., Mudelsee, M., 2022. The multifaceted history of the Walker Circulation during the Plio-Pleistocene. Quat. Sci. Rev. 286 https://doi.org/10.1016/j.quascirev.2022.107529.
Kaboth-Bahr, S., Gosling, W.D., Vogelsang, R., Bahr, A., Scerri, E.M.L., Asrat, A., Cohen, A.S., Dusing, W., Foerster, V., Lamb, H.F., Maslin, M.A., Roberts, H.M., Schabitz, F., Trauth, M.H., 2021. Paleo-ENSO influence on African environments and early modern humans. Proc. Natl. Acad. Sci. 118 https://doi.org/10.1073/pnas.2018277118.
Kao, S.-J., Jan, S., Hsu, S.-C., Lee, T.-Y., Dai, M., 2008. Sediment Budget in the Taiwan Strait with High Fluvial Sediment Inputs from Mountainous Rivers: New Observations and Synthesis. Terr. Atmos. Ocean. Sci. 19, 525. https://doi.org/10.3319/TAO.2008.19.5.525(Oc).
Kelman, I., 2013. Saffir–Simpson hurricane intensity scale. In: Bobrowsky, P.T. (Ed.), Encyclopedia of Natural Hazards. Springer, Netherlands, Dordrecht, pp. 882–883.
Knutson, T.R., McBride, J.L., Chan, J., Emanuel, K., Holland, G., Landsea, C., Held, I., Kossin, J.P., Srivastava, A.K., Sugi, M., 2010. Tropical cyclones and climate change. Nat. Geosci. 3, 157–163. https://doi.org/10.1038/ngeo779.
Laskar, J., Robutel, P., Joutel, F., Gastineau, M., Correia, A.C.M., Levrard, B., 2004. A long-term numerical solution for the insolation quantities of the Earth. Astron. Astrophys. 428, 261–285. https://doi.org/10.1051/0004-6361:20041335.
Lee, T.-Y., Huang, J.-C., Lee, J.-Y., Jien, S.-H., Zehetner, F., Kao, S.-J., 2015. Magnified Sediment Export of Small Mountainous Rivers in Taiwan: Chain Reactions from increased Rainfall Intensity under Global Warming. PLoS One 10, e0138283. https://doi.org/10.1371/journal.pone.0138283.
Li, L., Li, Q., Tian, J., Wang, P., Wang, H., Liu, Z., 2011. A 4-Ma record of thermal evolution in the tropical western Pacific and its implications on climate change. Earth Planet. Sci. Lett. 309, 10–20. https://doi.org/10.1016/j.epsl.2011.04.016.
Liautaud, P.R., Hodell, D.A., Huybers, P.J., 2020. Detection of significant climatic precession variability in early Pleistocene glacial cycles. Earth Planet. Sci. Lett. 536, 116137 https://doi.org/10.1016/j.epsl.2020.116137.
Lin, C.-H., 2000. Thermal modeling of continental subduction and exhumation constrained by heat flow and seismicity in Taiwan. Tectonophysics 324, 189–201. https://doi.org/10.1016/S0040-1951(00)00117-7.
Lin, C.-W., Chen, W.-S., 2016. Geological Map of Taiwan. Geological Society of Taiwan, Taipei, Taiwan.
Lin, A.T.-S., Watts, A.B., 2002. Origin of the West Taiwan basin by orogenic loading and flexure of a rifted continental margin. J. Geophys. Res. Solid Earth 107, 0148–0227. https://doi.org/10.1029/2001JB000669.
Lin, A.T., Watts, A.B., Hesselbo, S.P., 2003. Cenozoic stratigraphy and subsidence history of the South China Sea margin in the Taiwan region. Basin Res. 15, 453–478. https://doi.org/10.1046/j.1365-2117.2003.00215.x.
Lin, A.T., Wang, S.-M., Hung, J.-H., Wu, M.-S., Lui, C.S., 2007. Lithostratigraphy of the Taiwan Chelung-pu fault drilling project-a borehole and its neighboring region, Central Taiwan. Terr. Atmos. Ocean. Sci. 18.
Lisiecki, L.E., Raymo, M.E., 2005. A Pliocene-Pleistocene stack of 57 globally distributed benthic δ18O records. Paleoceanography 20. https://doi.org/10.1029/2004pa001071.

Lisiecki, L.E., Raymo, M.E., 2007. Plio–Pleistocene climate evolution: trends and transitions in glacial cycle dynamics. Quat. Sci. Rev. 26, 56–69. https://doi.org/10.1016/j.quascirev.2006.09.005.
Liu, S.C., Fu, C., Shiu, C.-J., Chen, J.-P., Wu, F., 2009. Temperature dependence of global precipitation extremes. Geophys. Res. Lett. 36 https://doi.org/10.1029/2009gl040218.
Liu, Y., Lo, L., Shi, Z., Wei, K.Y., Chou, C.J., Chen, Y.C., Chuang, C.K., Wu, C.C., Mii, H.S., Peng, Z., Amakawa, H., Burr, G.S., Lee, S.Y., DeLong, K.L., Elderfield, H., Shen, C.C., 2015. Obliquity pacing of the western Pacific Intertropical Convergence Zone over the past 282,000 years. Nat. Commun. 6, 10018. https://doi.org/10.1038/ncomms10018.
Liu, C., Nie, J., Li, Z., Qiao, Q., Abell, J.T., Wang, F., Xiao, W., 2021. Eccentricity forcing of East Asian monsoonal systems over the past 3 million years. Proc. Natl. Acad. Sci. U. S. A. 118 https://doi.org/10.1073/pnas.2107055118.
MacEachern, J.A., Dashtgard, S.E., Knaust, D., Catuneanu, O., Bann, K.L., Pemberton, S. G., 2012. Chapter 6 - Sequence Stratigraphy. In: Knaust, D., Bromley, R.G. (Eds.), Developments in Sedimentology. Elsevier, pp. 157–194.
Marshall, N., Zeeden, C., Hilgen, F., Krijgsman, W., 2017. Milankovitch cycles in an equatorial delta from the Miocene of Borneo. Earth Planet. Sci. Lett. 472, 229–240. https://doi.org/10.1016/j.epsl.2017.04.015.
Meyers, S.R., 2014. Astrochron: An R Package for Astrochronology. https://cran.r-project.org/package=astrochron.
Milankovitch, M., 1941. Kanon der Erdbestrahlung und Seine Andwendung auf das Eiszeiten-Problem, 133. Royal Serbian Academy, Belgrade, Serbia, p. 633.
Miller, K.G., Browning, J.V., Schmelz, W.J., Kopp, R.E., Mountain, G.S., Wright, J.D., 2020. Cenozoic Sea-level and cryospheric evolution from deep-sea geochemical and continental margin records. Sci. Adv. 6 https://doi.org/10.1126/sciadv.aaz1346 eaaz1346.
Milliman, J.D., Meade, R.H., 1983. World-wide delivery of river sediment to the oceans. J. Geol. 91, 1–21.
Milliman, J.D., Lin, S.W., Kao, S.J., Liu, J.P., Liu, C.S., Chiu, J.K., Lin, Y.C., 2007. Short-term changes in seafloor character due to flood-derived hyperpycnal discharge: Typhoon Mindulle, Taiwan, July 2004. Geology 35, 779–782. https://doi.org/10.1130/G23760A.1.
Milliman, J.D., Lee, T.Y., Huang, J.C., Kao, S.J., 2017. Impact of catastrophic events on small mountainous rivers: Temporal and spatial variations in suspended- and dissolved-solid fluxes along the Choshui River, central western Taiwan, during typhoon Mindulle, July 2–6, 2004. Geochim. Cosmochim. Acta 205, 272–294. https://doi.org/10.1016/j.gca.2017.02.015.
Nagel, S., Castelltort, S., Wetzel, A., Willett, S.D., Mouthereau, F., Lin, A.T., 2013. Sedimentology and foreland basin paleogeography during Taiwan arc continent collision. J. Asian Earth Sci. 62, 180–204. https://doi.org/10.1016/j.jseaes.2012.09.001.
Nagel, S., Granjeon, D., Willett, S., Lin, A.T.-S., Castelltort, S., 2018. Stratigraphic modeling of the Western Taiwan foreland basin: Sediment flux from a growing mountain range and tectonic implications. Mar. Pet. Geol. 96, 331–347. https://doi.org/10.1016/j.marpetgeo.2018.05.034.
Naish, T.R., Abbott, S.T., Alloway, V., Beu, A.G., Carter, R.M., Edwards, A.R., Journeaux, T.D., Kamp, P.J.J., Pillans, B.J., Saul, G., Woolfe, K.J., 1998. Astronomical calibration of a southern hemisphere Plio-Pleistocene reference section, Wanganui Basin, New Zealand. Quat. Sci. Rev. 17, 695–710. https://doi.org/10.1016/S0277-3791(97)00075-9.
Nayak, K., Garzanti, E., Lin, A.T.S., Castelltort, S., 2022. Taiwan river muds from source to sink: Provenance control, inherited weathering, and offshore dispersal pathways. Sediment. Geol. https://doi.org/10.1016/j.sedgeo.2022.106199.
Pagani, M., Liu, Z., LaRiviere, J., Ravelo, A.C., 2009. High Earth-system climate sensitivity determined from Pliocene carbon dioxide concentrations. Nat. Geosci. 3, 27–30. https://doi.org/10.1038/ngeo724.
Pan, T.Y., Lin, A.T.S., Chi, W.R., 2015. Paleoenvironments of the evolving Pliocene to early Pleistocene foreland basin in northwestern Taiwan: an example from the Dahan River section. Island Arc 24, 317–341. https://doi.org/10.1111/iar.12113.
Pancost, R.D., 2017. Climate change narratives. Nat. Geosci. 10, 466–468. https://doi.org/10.1038/ngeo2981.
Paola, C., Ganti, V., Mohrig, D., Runkel, A.C., Straub, K.M., 2018. Time not our time: physical controls on the preservation and measurement of geologic time. Annu. Rev. Earth Planet. Sci. 46, 409–438. https://doi.org/10.1146/annurev-earth-082517-010129.
Peduzzi, P., Chatenoux, B., Dao, H., De Bono, A., Herold, C., Kossin, J., Mouton, F., Nordbeck, O., 2012. Global trends in tropical cyclone risk. Nat. Clim. Chang. 2, 289–294. https://doi.org/10.1038/nclimate1410.
Raymo, M.E., Nisancioglu, K.H., 2003. The 41 kyr world: Milankovitch's other unsolved mystery. Paleoceanography 18. https://doi.org/10.1029/2002PA000791.
R Core Team, 2022. R: A Language and Environment for Statistical Computing. R Foundation for Statistical Computing, Vienna, Austria. https://www.R-project.org/.
Raymo, M.E., Lisiecki, L.E., Nisancioglu, K.H., 2006. Plio-pleistocene ice volume, antarctic climate, and the global δ18o record. Science 313, 492–495. https://doi.org/10.1126/science.1123296.
Read, J.F., Li, M., Hinnov, L.A., Nelson, C.S., Hood, S., 2020. Testing for astronomical forcing of cycles and gamma ray signals in outer shelf/upper slope, mixed siliciclastic-carbonates: upper Oligocene, New Zealand. Palaeogeogr. Palaeoclimatol. Palaeoecol. 555, 109821 https://doi.org/10.1016/j.palaeo.2020.109821.
Rohde, R.A., 2006. Historical Tropical Cyclone Tracks. NASA Earth Observatory.
Rohling, E.J., Foster, G.L., Grant, K.M., Marino, G., Roberts, A.P., Tamisiea, M.E., Williams, F., 2014. Sea-level and deep-sea-temperature variability over the past 5.3 million years. Nature 508, 477–482. https://doi.org/10.1038/nature13230.
Sadler, P.M., 1981. Sediment Accumulation rates and the Completeness of Stratigraphic Sections. J. Geol. 89, 569–584.
Savin, S.M., Douglas, R.G., Stehli, F.G., 1975. Tertiary marine paleotemperatures. GSA. Bulletin 86, 1499–1510. https://doi.org/10.1130/0016-7606(1975)86<1499:Tmp>2.0.Co;2.
Schlumberger, 1989. Log Interpretation Principles/Applications. Houston, Schlumberger, p. 233.
Shackleton, N., 1967. Oxygen Isotope analyses and Pleistocene Temperatures Re-assessed. Nature 215, 15–17. https://doi.org/10.1038/215015a0.
Shackleton, N.J., Berger, A., Peltier, W.R., 1990. An alternative astronomical calibration of the lower Pleistocene timescale based on ODP Site 677. Trans. R. Soc. Edinb. Earth Sci. 81, 251–261. https://doi.org/10.1017/S0263593300020782.
Shackleton, N.J., Hagelberg, T.K., Crowhurst, S.J., 1995. Evaluating the success of astronomical tuning: pitfalls of using coherence as a criterion for assessing pre-Pleistocene timescales. Paleoceanography 10, 693–697. https://doi.org/10.1029/95PA01454.
Shao, X., Wang, T., Wang, Y., Cheng, H., Zhao, K., Kong, X., 2020. ENSO-Like Pacing of the Asian Summer Monsoon during the early Holocene. J. Meteorol. Res. 34, 325–335. https://doi.org/10.1007/s13351-020-9079-9.
Sinnesael, M., Loi, A., Dabard, M.-P., Vandenbroucke, T.R.A., Claeys, P., 2022. Cyclostratigraphy of the Middle to Upper Ordovician successions of the Armorican Massif (western France) using portable X-ray fluorescence. Geochronology 4, 251–267. https://doi.org/10.5194/gchron-4-251-2022.
Tabor, C.R., Poulsen, C.J., Pollard, D., 2015. How obliquity cycles powered early Pleistocene global ice-volume variability. Geophys. Res. Lett. 42, 1871–1879. https://doi.org/10.1002/2015gl063322.
Tory, K.J., Frank, W.M., 2012. Tropical Cyclone Formation, Global Perspectives on Tropical Cyclones. World Scientific, pp. 55–91.
Tung, Y.-S., Wang, S.-Y.S., Chu, J.-L., Wu, C.-H., Chen, Y.-M., Cheng, C.-T., Lin, L.-Y., 2020. Projected increase of the East Asian summer monsoon (Meiyu) in Taiwan by climate models with variable performance. Meteorol. Appl. 27, e1886 https://doi.org/10.1002/met.1886.
Ulfers, A., Hesse, K., Zeeden, C., Russell, J.M., Vogel, H., Bijaksana, S., Wonik, T., 2021. Cyclostratigraphy and paleoenvironmental inference from downhole logging of sediments in tropical Lake Towuti, Indonesia. J. Paleolimnol. 65, 377–392. https://doi.org/10.1007/s10933-020-00171-9.
Ulfers, A., Zeeden, C., Wagner, B., Krastel, S., Buness, H., Wonik, T., 2022. Borehole logging and seismic data from Lake Ohrid (North Macedonia/Albania) as a basis for age-depth modelling over the last one million years. Quat. Sci. Rev. 276 https://doi.org/10.1016/j.quascirev.2021.107295.
van der Lubbe, H.J.L., Hall, I.R., Barker, S., Hemming, S.R., Baars, T.F., Starr, A., Just, J., Backeberg, B.C., Joordens, J.C.A., 2021. Indo-Pacific Walker circulation drove Pleistocene African aridification. Nature 598, 618–623. https://doi.org/10.1038/s41586-021-03896-3.
Vaucher, R., Dashtgard, S.E., Horng, C.-S., Zeeden, C., Dillinger, A., Pan, Y.-Y., Setiaji, R. A., Chi, W.-R., Löwemark, L., 2021. Insolation-paced sea level and sediment flux during the early Pleistocene in Southeast Asia. Sci. Rep. 11, 16707. https://doi.org/10.1038/s41598-021-96372-x.
Wang, Q., Li, J., Jin, F.-F., Chan, J.C.L., Wang, C., Ding, R., Sun, C., Zheng, F., Feng, J., Xie, F., Li, Y., Li, F., Xu, Y., 2019. Tropical cyclones act to intensify El Niño. Nat. Commun. 10 https://doi.org/10.1038/s41467-019-11720-w.
Westerhold, T., Marwan, N., Drury, A.J., Liebrand, D., Agnini, C., Anagnostou, E., Barnet, J.S.K., Bohaty, S.M., De Vleeschouwer, D., Florindo, F., Frederichs, T., Hodell, D.A., Holbourn, A.E., Kroon, D., Lauretano, V., Littler, K., Lourens, L.J., Lyle, M., Pälike, H., Röhl, U., Tian, J., Wilkens, R.H., Wilson, P.A., Zachos, J.C., 2020. An astronomically dated record of Earth's climate and its predictability over the last 66 million years. Science 369, 1383–1387. https://doi.org/10.1126/science.aba6853.
Wilkens, R.H., Westerhold, T., Drury, A.J., Lyle, M., Gorgas, T., Tian, J., 2017. Revisiting the Ceara rise, equatorial Atlantic Ocean: isotope stratigraphy of ODP Leg 154 from 0 to 5 Ma. Clim. Past 13, 779–793. https://doi.org/10.5194/cp-13-779-2017.
Worthington, P.F., 1990. Sediment cyclicity from well logs. Geol. Soc. Lond., Spec. Publ. 48, 123–132. https://doi.org/10.1144/gsl.Sp.1990.048.01.11.
Wu, L., Liang, J., Wu, C.-C., 2011. Monsoonal Influence on Typhoon Morakot (2009). Part I: Observational Analysis. J. Atmos. Sci. 68, 2208–2221. https://doi.org/10.1175/2011JAS3730.1.
Yan, Q., Wei, T., Zhang, Z., Jiang, N., 2019. Orbitally Induced Variation of Tropical Cyclone Genesis potential over the Western North Pacific during the Mid-Piacenzian warm period: a Modeling Perspective. Paleoceanography Paleoclimatol. 34, 902–916. https://doi.org/10.1029/2018pa003535.
Yu, H.-S., Chou, Y.-W., 2001. Characteristics and development of the flexural forebulge and basal unconformity of Western Taiwan Foreland Basin. Tectonophysics 333, 277–291. https://doi.org/10.1016/S0040-1951(00)00279-1.
Zachos, J., Pagani, M., Sloan, L., Thomas, E., Billups, K., 2001. Trends, Rhythms, and Aberrations in Global climate 65 Ma to present. Science 292, 686–693. https://doi.org/10.1126/science.1059412.
Zeebe, R.E., Ridgwell, A., Zachos, J.C., 2016. Anthropogenic carbon release rate unprecedented during the past 66 million years. Nat. Geosci. 9, 325–329. https://doi.org/10.1038/ngeo2681.
Zeeden, C., Hilgen, F., Westerhold, T., Lourens, L., Röhl, U., Bickert, T., 2013. Revised Miocene splice, astronomical tuning and calcareous plankton biochronology of ODP Site 926 between 5 and 14.4Ma. Palaeogeogr. Palaeoclimatol. Palaeoecol. 369, 430–451. https://doi.org/10.1016/j.palaeo.2012.11.009.

Zeeden, C., Meyers, S.R., Hilgen, F.J., Lourens, L.J., Laskar, J., 2019. Time scale evaluation and the quantification of obliquity forcing. Quat. Sci. Rev. 209, 100–113. https://doi.org/10.1016/j.quascirev.2019.01.018.

Zhang, X., Wu, M., Liu, Y., Hao, Z., Zheng, J., 2018. The relationship between the East Asian Summer Monsoon and El Niño-Southern Oscillation revealed by reconstructions and a control simulation for millennium. Quat. Int. 493, 106–113. https://doi.org/10.1016/j.quaint.2018.06.024.

Zhang, G., Murakami, H., Knutson, T.R., Mizuta, R., Yoshida, K., 2020. Tropical cyclone motion in a changing climate. Sci. Adv. 6 https://doi.org/10.1126/sciadv.aaz7610 eaaz7610.